Research Article

A Simple and Reliable Synthesis of Superparamagnetic Magnetite Nanoparticles by Thermal Decomposition of Fe(acac)$_3$

C. Toyos-Rodríguez,[1,2] **J. Calleja-García,**[1] **L. Torres-Sánchez** ![ORCID],[1,2] **A. López,**[1]
Ahmed M. Abu-Dief,[3] **A. Costa,**[4] **L. Elbaile,**[2] **R. D. Crespo,**[2] **J. S. Garitaonandia,**[5] **E. Lastra,**[1]
J. A. García ![ORCID],[2] **and F. J. García-Alonso**[1]

[1]*Departamento de Química Orgánica e Inorgánica, c/ Julián Clavería, 8, 33006 Oviedo, Spain*
[2]*Departamento de Física, Universidad de Oviedo, c/ Calvo Sotelo s/n, 33007 Oviedo, Spain*
[3]*Chemistry Department, Faculty of Science, Sohag University, 82524-Sohag, Egypt*
[4]*Departamento de Química Analítica y Química Física, c/ Julián Clavería, 8, 33006 Oviedo, Spain*
[5]*Fisika Aplicatua II Saila, Euskal Erriko Unibertsitatea, Alameda Urquijo s/n 48013 Bilbao, Spain*

Correspondence should be addressed to J. A. García; joseagd@uniovi.es

Magnetic nanoparticles have been largely proposed as means of technological tools due to its value in different fields, especially in biomedicine. Herein, we present a robust, highly reproducible and low-cost method to obtain superparamagnetic magnetite nanoparticles (MNP-II) of about 15 ± 5 nm diameter by thermal decomposition of [Fe(acac)$_3$] in a one-pot, two-step method. In the first step, magnetite nanoparticles (MNP-I) of lower size, 9 ± 4 nm, with a saturation magnetization (M_S) of 65 emu/g and a coercive field (H_c) of 1 Oe are obtained. In the second step, those particles MNP-I act as seeds for the final MNP-II which present a saturation magnetization of 70 emu/g and a coercive field of 12 Oe.

1. Introduction

Magnetic nanoparticles have been of interest and a constant subject of study since the 1970s from the scientific point of view (due to their unique electrical, magnetic, and chemical properties) and from their technological applications in different fields including catalysis [1], data storage devices [2], and environmental remediation [3]. However, the main effort in developing magnetic nanoparticles is due to their application in biomedicine to be used in biosensors, magnetic resonance imaging, drug transport, and treatment of tumors by hyperthermia [4–6].

The size of the magnetic nanoparticles is crucial in biomedicine as it affects cellular uptake, biodistribution, and other pharmacokinetic parameters.

The control of the size of the particles is also fundamental to avoid the effect of the immune system because nanoparticles with a hydrodynamic diameter lower than 5.5 nm are

rapidly excreted through the kidney [7], while large nanoparticles (hydrodynamic diameter > 100 nm) are rapidly taken up by the phagocytes and tend to accumulate in the liver and spleen [8, 9]. According to the abovementioned information, the diameter of interest for particles in biomedical applications is between 20 nm and 100 nm, since these particles tend to accumulate into tumors [10, 11].

Among the different magnetic nanoparticles, iron oxide nanoparticles (IONPs) have been extensively studied due to their simple synthesis, low toxicity, affordability, stability under extreme conditions, and polar surface [12].

In addition, the magnetic properties of magnetite nanoparticles depend on their size, being superparamagnetic when they are smaller than 20 nm [13] but increasing their saturation magnetization with their radius [14]. This magnetic behavior is fundamental from the point of view of their application in medicine because if the particles were not superparamagnetic, they would continue attracting each

other after removing the external magnetic field, forming aggregates inside the organism, which would be rapidly taken up by the phagocytes [8] and in addition tend to produce embolism [15].

A large number of synthetic routes have been developed to produce IONPs of different sizes and shapes [16], with the thermal decomposition of iron complexes being one of the most widely used [17], which provides good size controllability and high crystallinity. Park et al. [18] described, in 2004, an excellent method to obtain variable amounts of IONPs of desired and uniform size by heating iron oleate in different solvents. However, the sophistication of the used heating rate device and the convenience of a more stable starting material limit its general acceptance. Due to that, the development of new procedures to prepare magnetite (Fe$_3$O$_4$) nanoparticles has been widely studied in the last decade [19, 20]. In particular, there is a permanent interest in preparing, in a simple way, MNP under 20 nm diameter (to avoid ferrimagnetic behavior) but close to this size in order to enhance their saturation magnetization. On the other hand, obtaining a reproducible, low-cost methodology that provides the same results as more expensive ones is desirable.

Benzyl ether has been widely used as solvent for the synthesis of iron oxide nanoparticles starting from iron (III) acetylacetonate using three [21, 22], two [23, 24], or one extra additive [25, 26]. Oleylamine and oleic acid have been proved as good surfactants, with the ratio of oleylamine/oleic acid being an important factor in determining both the size and the shape of the MNP [24].

A robust, one-pot, two-step method is presented here to obtain magnetite nanoparticles, MNP-II, of about 15 ± 5 nm diameter, heating Fe(acac)$_3$ in benzyl ether in the presence of oleic acid and oleylamine by using a noncomplex heating equipment. Moreover, at the end of the first step, that is, after refluxing the initial mixture for 15 minutes, smaller magnetic nanoparticles, MNP-I, of about 9 ± 4 nm diameter with a M_S of 65 emu/g are formed. They could be isolated or eventually be converted into seeds [27] for the final product, if the flask is cooled down to room temperature and then refluxed for two additional hours.

2. Materials and Methods

2.1. Materials. Benzyl ether (C$_{14}$H$_{14}$O, 98%), oleic acid (C$_{18}$H$_{34}$O$_2$, 99.99%), iron (III) acetylacetonate (C$_{15}$H$_{21}$FeO$_6$, 97%), toluene (C$_7$H$_8$, 99.8%), and ethyl acetate (C$_4$H$_8$O$_2$, 99.8%) were obtained from Sigma-Aldrich; 2-propanol (C$_3$H$_8$O, 99.99%) and petroleum ether (40°-60°) were supplied by VWR chemicals while oleylamine (C$_{18}$H$_{37}$N, 80-90%) was purchased from Acros Organics. All the reactions were carried out under inert atmosphere of argon.

2.2. Experimental Procedure. Iron (III) acetylacetonate (1.42 g, 4.0 mmol) was dispersed in a mixture of dibenzyl ether (20 ml), oleylamine (2.8 ml, 2.27 g, 7.21 mmol), and oleic acid (2.7 ml, 2.39 g, 8.46 mmol) previously deoxygenated (bubbling Ar through the mixture for 30 minutes) in a three-necked round-bottom 250 ml flask. The suspension
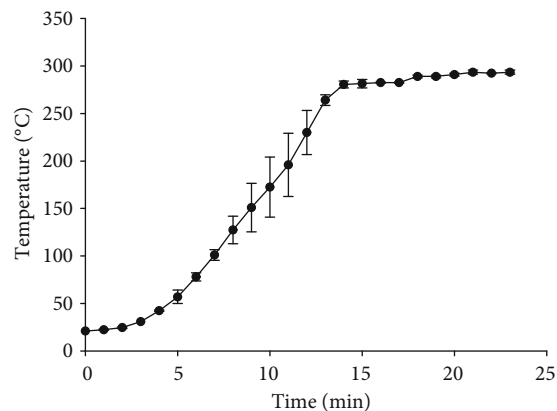

FIGURE 1: Temperature of the vapor condensed at the thermometer bulb placed in the third neck of the reaction flask along the reaction time.

was heated with vigorous mechanical stirring until the refluxing temperature was reached and then maintained for 15 minutes under the same conditions. Afterwards, the heating mantle was removed and the reaction temperature slowed down to room temperature. At this point, two different routes were followed to obtain two different types of MNP.

2.2.1. Procedure A: Isolation of MNP-I. While the formed black magnetite nanoparticles were retained with an external magnetic disk, the supernatant suspension was removed. Later, the nanoparticles were washed successively with a mixture 1 : 1 (in volume) of 2-propanol and light petroleum ether (4 × 20 ml) and finally dried in vacuum to give 130 mg of MNP-I (14% yield).

2.2.2. Procedure B: Preparation of MNP-II. The mixture was then refluxed for two other hours. Afterwards, the resulting black magnetite nanoparticles were isolated and purified in a similar way giving 270 mg of MNP-II (29% yield).

Both reactions have been carried out by several coauthors more than ten times along a year with comparable results. (Occasionally, the nanoparticles were slightly contaminated with silicone used in the glass stirrer gland that provides a vapor-tight seal between the paddle and the flask. The silicone was effectively eliminated washing the sample with a 2 : 1 (in volume) mixture of ethyl acetate and toluene.)

2.3. Characterization. Fourier transform infrared spectroscopic (FT-IR) measurements were performed on a FT-IR Spectrometer Paragon 1000 from PerkinElmer (USA) using KBr pressed disks.

Scanning electron microscopy images were obtained using a JEOL-6610 with an accelerating voltage of 20 kV.

Transmission electron microscopy images were obtained using either a JEOL JEM 2100F HRTEM (for MNP-I) or a JEOL-2000 EX-II TEM (for MNP-II) on a copper grid, using an accelerating voltage of 200 or 160 kV, respectively. The calculations for the size estimation were obtained with the ImageJ software, by measuring the largest dimension of each particle.
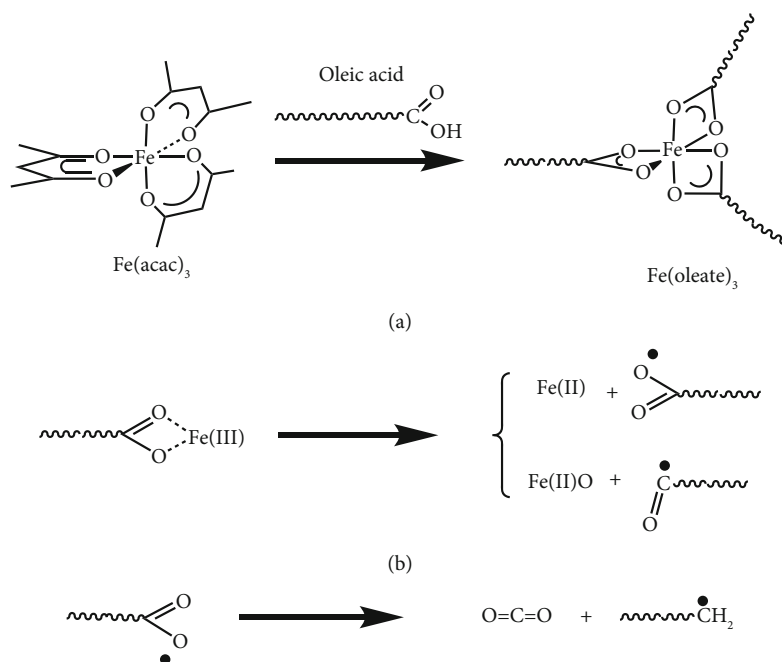
Scheme 1: Reaction mechanisms of the formation of magnetite nanoparticles using as precursors iron (III) acetylacetonate and oleic acid.

X-ray powder diffraction (XRPD) data for the two kinds of particles were collected, at RT, using CuKα1,2 radiation (λ = 1.54056 Å and 1.54439 Å) in a Bragg-Brentano reflection configuration, on an PHILIPS X' PERT PRO Panalytical diffractometer in a 2θ range of 15–90°, with a step size of 0.03. In order to obtain the instrumental broadening contribution and deconvolution, the line profile function, pure iron (II; III) oxide (Puratronic®) with high crystallinity, has been used as external reference.

Magnetization measurements at room temperature and zero-field-cooled and field-cooled were performed using a PPMS-14T (Physical Property Measurement System). This system allows applying magnetic fields to the samples up to 14 T, by using superconducting coils, at a range of temperatures from 1.9 K to 400 K.

Mössbauer spectroscopy measurements were carried out in transmission geometry using a conventional constant-acceleration spectrometer with 57Co-Rh source. Spectra were collected at different temperatures under high vacuum (10−5 torr) in a commercial Oxford Instruments cryostat. The isomer shift values were taken with respect to an α-Fe calibration foil measured at room temperature. NORMOS program was used for fitting the spectra.

3. Results and Discussion

3.1. Structural Characterization. Decomposition of iron (III) acetylacetonate in boiling benzyl ether under argon atmosphere in the presence of oleic acid and oleylamine provides two types of black superparamagnetic nanoparticles of magnetite MNP-I and MNP-II, depending on the reaction conditions.
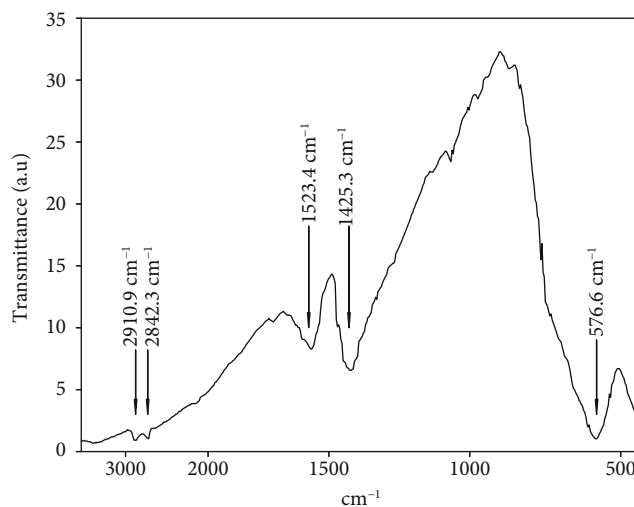

Figure 2: Infrared spectrum of the magnetic nanoparticles of step 1 (MNP-I).

The control of the heating rate seems to be of paramount importance for determining the size of the iron oxide nanoparticles [28]. In our case, the heating rate of the reaction was followed indirectly by the temperature variations of the vapor condensed in the thermometer bulb placed in the third neck of the flask (the other two were occupied by the reflux condenser and the stirring paddle). The resulting curve, shown in Figure 1, is markedly reproducible for all the reactions we have monitored.

The size mechanism control of the heating-up method should be regulated by two processes. The first is the "burst nucleation" when a great number of nuclei are formed. Although after the burst nucleation some particles are greater
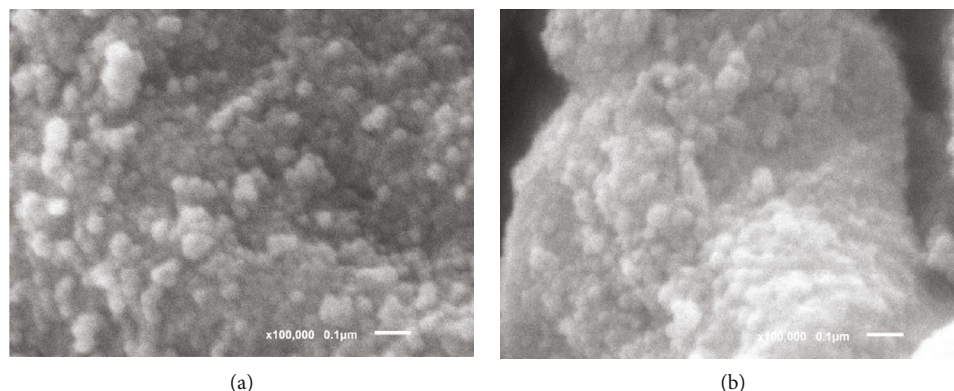
(a)

(b)

FIGURE 3: SEM images of the nanoparticles: (a) MNP-I and (b) MNP-II.

than others, it is not of special concern as in the second process, the "size focusing," small particles grow faster than big particles [29], reaching all the same size.

The first observed stage in the heating ramp is detected at about 117°C, and it is accompanied by the appearance of a white cloud. The existence of this white cloud has been related to the presence of water vapor. Water should be released during the ketonization of oleic acid at elevated temperatures [30]. The second stage is located around 220°C and could be associated to the formation of the magnetite nucleus [31]. The formation of magnetite starting from $Fe(acac)_3$ could follow the currently accepted mechanism. Initially, the acetylacetonate ligand should be replaced by the oleate group (A in Scheme 1) [31]; then, the decomposition of iron oleate would result in the breakage of M-O and MO-C bonds of metal carboxylate and the partial reduction to Fe(II) (B in Scheme 1) [32] and the subsequent decarboxylation and formation of organic radicals (C in Scheme1) [30].

The infrared spectra of MNP-I and MNP-II are the same. Figure 2shows the infrared spectrum of MNP-I. The characteristic absorption bands of the oleate coating are at 2911 cm^{-1}, w, and 2842 cm^{-1}, w (stretching CH), and at 1523 cm^{-1}, w, br, and 1425 cm^{-1}, m, br (antisymmetric and symmetric stretching of the carboxylate group) [33]. The band at 1425 cm^{-1} should also include some contribution of the CH_2 deformation absorption. Besides, there exists another strong, broad band at 577 cm^{-1}, due to magnetite solid-state vibrations. (The occasional presence of small amounts of silicone is detected by the apparition of its characteristic bands at 1258, 1092, 1018, and 797 cm^{-1}.)

The morphology and size distribution of the nanoparticles have been obtained by SEM and TEM. SEM images of the nanoparticles are shown in Figure 3. They give an overall view on a wide area which allows to see that no large particles have been produced [34]. The particles showed a high degree of agglomeration due to dipole-dipole interaction [35].

The diameter of nanoparticles determined by TEM is 9 ± 4 nmfor MNP-I and 15 ± 5 nm for MNP-II. In Figure 4, a micrograph as well as the size distribution of both kinds of nanoparticles is shown.

The X-ray diffraction pattern of MNP-I and MNP-II shows the characteristic diffraction peaks of the magnetite (see Figure 5) with the samples not being totally crystalline

as an initial elevation of the patterns was registered. The 2θ diffraction angles and the lattice spacing d (Å) of our sample are collected in Table 1. For comparative purposes, the standard atomic spacing for Fe_3O_4 are also included as well as the respective hkl indexes [26, 27].

The estimation of the crystalline size of magnetic nanoparticles has been carried out by using the FullProf program [36]. The effect of instrumental peak broadening was corrected by performing a Le Bail fitting method [37]. During the Le Bail fitting for each sample, instrumental parameters U, V, and W were kept constant, as well as the asymmetric parameters (SL and DL). The Thompson-Cox-Hastings pseudo-Voigt profile function expressed by a weighted sum of Gaussian and Lorentzian was applied to obtain the average apparent crystalline size directly [38]. From this estimation, an average apparent size (Figure 6) of 8 ± 3 nm and 12 ± 2 nm from MNP-I and MNP-II, respectively, is obtained. These results show that the crystallite and nanoparticle sizes are the same, indicating that both kinds of particles are monocrystallines.

3.2. Magnetic Characterization. The room temperature hysteresis loops of the particles obtained in the first step and in the second one step are shown in Figure 7. The magnetic behavior of the particles of the first step differs slightly from that observed in the final particles. The particles of the first step present superparamagnetic behavior with a coercive field of about 1 Oe at room temperature, and they also have a high saturation magnetization of about 65 emu/g. In the case of the final particles, the superparamagnetic behavior is slightly different. The coercive field has increased to a value of about 12 Oe; nevertheless, they are within the limits accepted as superparamagnetic. Also, it can be observed that there is an increase of the saturation magnetization, which in this case results in about 70 emu/g, lower than that of the bulk magnetite (92 emu/g). This decrease is not clear and is still the object of research. Now, different studies attribute this decrease to the surface spin canting [39, 40]. The saturation magnetization of both kinds of particles is really a high value and makes them very promising for their coating and subsequent use.

Magnetization curves of zero-field-cooled (ZFC) and field-cooled (FC) were measured in the temperature range
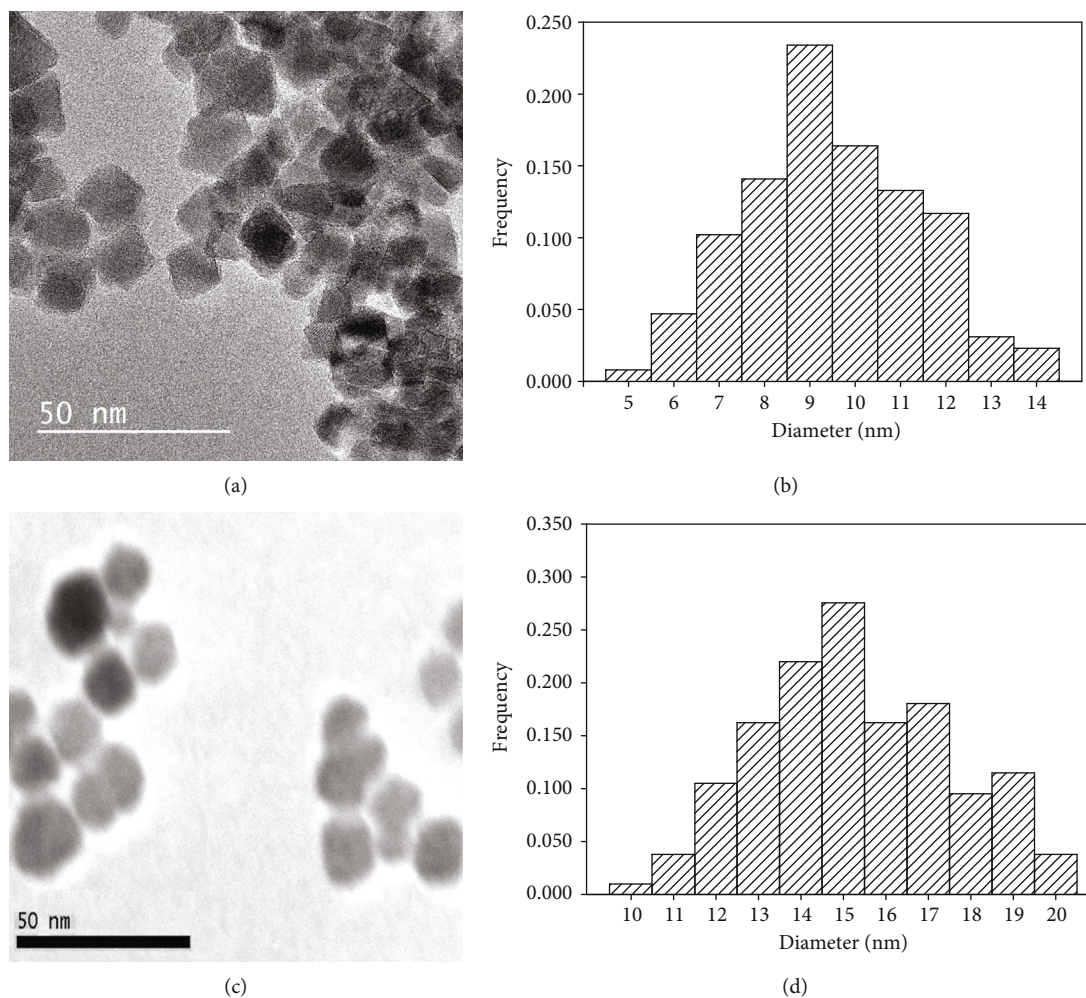
(a)

(b)

(c)

(d)

FIGURE 4: Representative TEM images (a, c) and size distribution (b, d) for MNP-I and MNP-II, respectively.
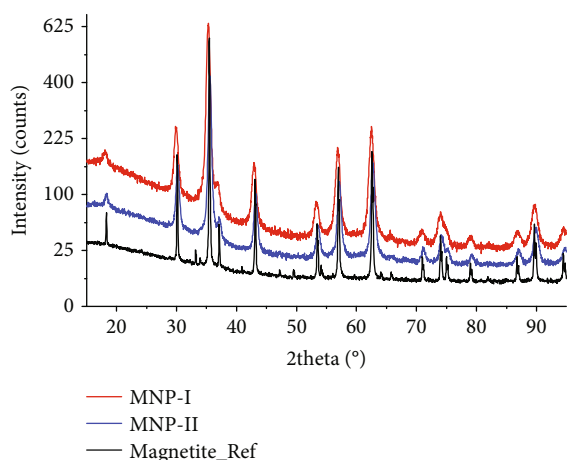

FIGURE 5: X-ray diffraction (XRD) pattern of MNP-I (red), MNP-II (blue), and reference magnetite (black).

from 5 K to 315 K. The samples were mounted in the PPMS at room temperature and cooled down to 5 K without applied field. After cooling, a dc field of 100 Oe was applied and the temperature was increased to 315 K.

The magnetic behavior of the two kinds of nanoparticles (Figure 8) differs slightly. MNP-I particles show a superparamagnetic behavior at room temperature with a coercive field minor than 1 Oe and saturation magnetization of 65 emu/g. The MNP-II particles present a coercive field of 12 Oe, a saturation magnetization of 70 emu/g, and a $T_B > 300$ K. On the other hand, the two kinds of nanoparticles show a Verwey transition at about 120 K. This anomalous behavior shown in the obtained curves has been studied by Bohra et al. [41], and it was explained by the nonspherical morphology of the samples.

Figure 9 shows the Mössbauer spectra of the studied samples obtained at different temperatures. For a better comparison, all the spectra are normalized to present the same area. The thermal evolution of the spectra strongly depends on the size of the MNPs.

The formal composition of magnetite can be written as $[Fe^{3+}]_A[Fe^{2+}Fe^{3+}]_BO^{2-}_4$, where A denotes Fe sites surrounded by oxygen ions forming tetrahedral and B corresponds to the Fe ions inside octahedral formed by the nearest oxygen ions. This structure is clearly reflected in the Mössbauer spectra obtained at 295 K and 150 K. The spectra have been fitted by two sextets presenting hyperfine parameters and a 1 : 2

TABLE 1: Experimental 2θ values and lattice spacing of MNP-I and MNP-II; Standard lattice spacing and corresponding plane assignation of Fe_3O_4.

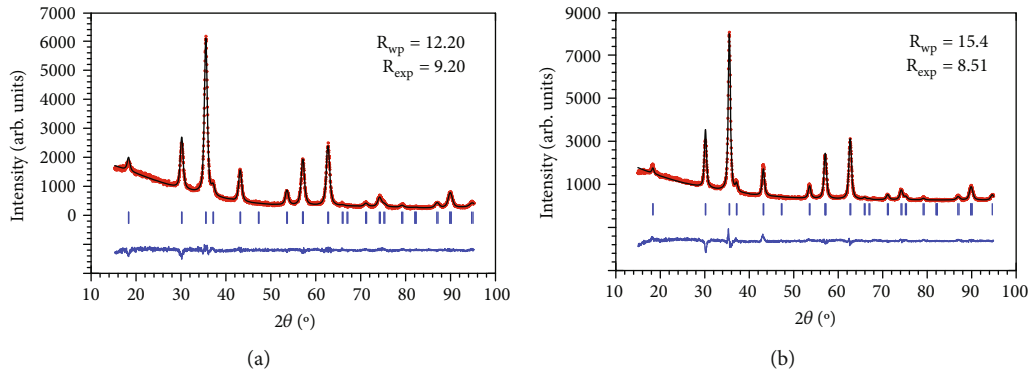| MNP-I	2θ (°)	17.6	30.0	35.4	37.0	43.2	53.7	57.1	62.6	71.2	73.9	79.3
	d (Å)	5.04	2.98	2.54	2.43	2.09	1.72	1.61	1.48	1.32	1.28	1.21
MNP-II	2θ (°)	18.3	30.2	35.5	37.1	43.2	53.5	57.1	62.7	71.1	74.2	79.2
	d (Å)	4.84	2.96	2.52	2.42	2.09	1.71	1.61	1.48	1.32	1.28	1.21
Standard values	Fe_3O_4	4.86	2.98	2.53	2.43	2.10	1.71	1.62	1.48	1.33	1.28	1.21
	hkl	111	220	311	222	400	422	511	440	620	533	444

FIGURE 6: Le Bail fitting (black line) and experimental data (red points) collected from MNP-I (a) and MNP-II (b).
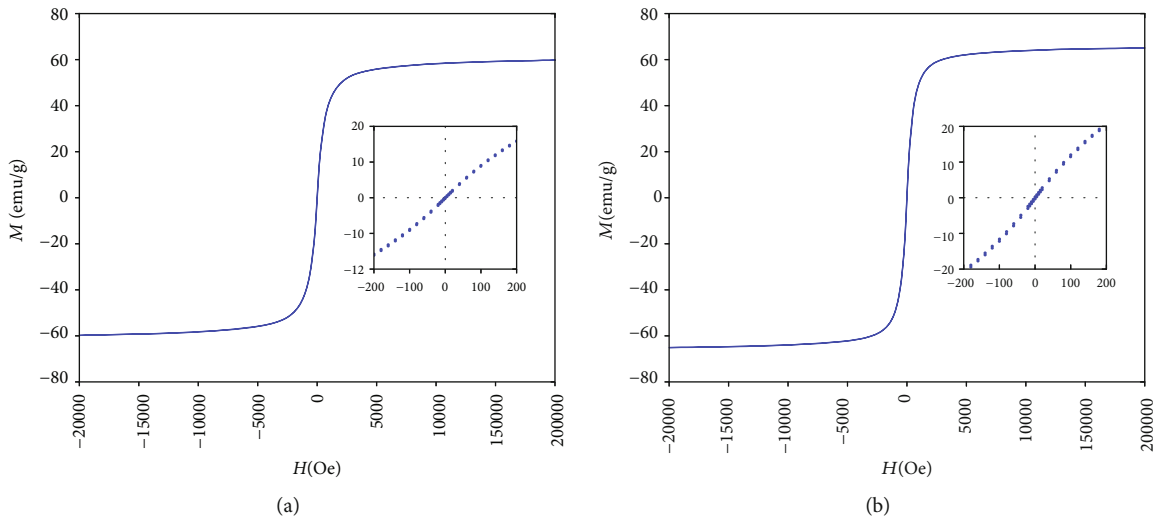

FIGURE 7: Magnetic hysteresis loops of the particles measured at room temperature: (a) first step and (b) second step. In the inset, an amplification of the low-field region of the hysteresis loops is shown.
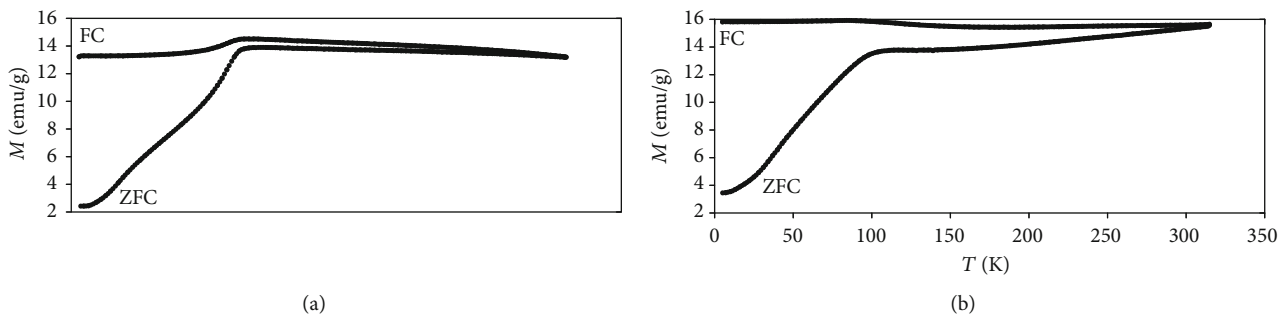

FIGURE 8: Results of the ZFC and FC magnetization measurements for the samples at an applied field of 100 Oe: (a) NPM-I and (b) NPM-II.
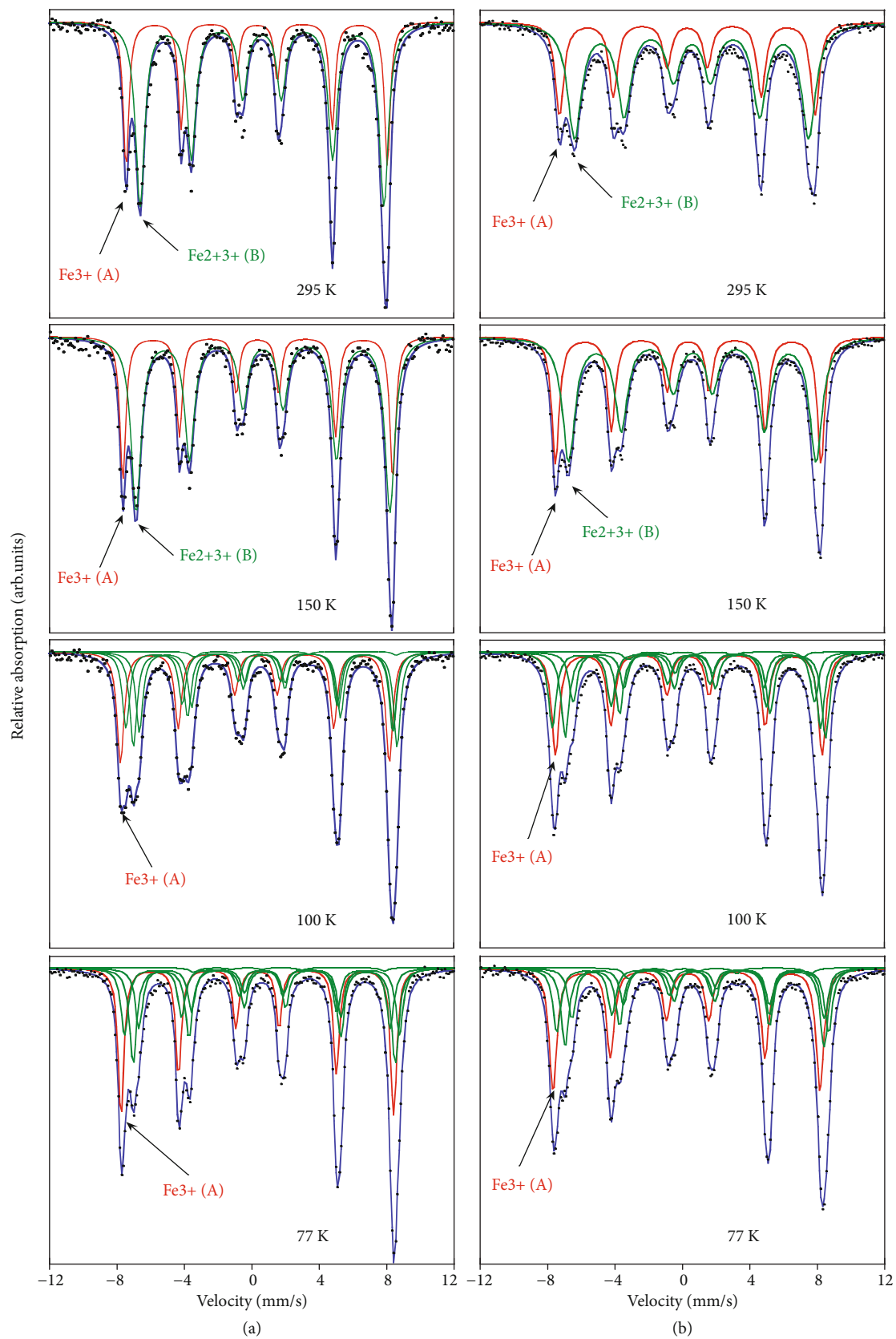
Figure 9: Mössbauer spectra of (a) MNP-I nanoparticles and (b) MNP-II nanoparticles.

TABLE 2: Isomer shift (IS), quadrupolar splitting (QS), hyperfine field (B_{hf}), and full width at half maximum (WID) values obtained from the fittings of the Mossbauer spectra of the study samples. %Fe denotes the obtained ratio of the resonant areas among Fe^{3+} A sites and the $Fe^{2+/3+}$ B sites of the magnetite.

(a)

| T (K) | Position | MNP-I | | | | |
		IS (mm/s)*	QS (mm/s)	B_{hf} (T)	WID (mm/s)	%Fe
295	Magnetite Fe^{3+} (A)	0.32 (1)	0.00 (1)	47.0 (1)	0.61 (1)	34 (1)
	Magnetite $Fe^{2+}Fe^{3+}$ (B)	0.59 (1)	-0.02 (1)	43.1 (1)	1.00 (1)	66 (1)
150	Magnetite Fe^{3+} (A)	0.38 (1)	0.00 (1)	48.9 (2)	0.53 (1)	37 (1)
	Magnetite $Fe^{2+}Fe^{3+}$ (B)	0.64 (1)	-0.03 (1)	45.5 (1)	0.90 (1)	63 (1)

(b)

| T (K) | Position | MNP-II | | | | |
		IS (mm/s)*	QS (mm/s)	B_{hf} (T)	WID (mm/s)	%Fe
295	Magnetite Fe^{3+} (A)	0.30 (1)	0.00 (3)	48.1 (1)	0.41 (1)	34 (1)
	Magnetite $Fe^{2+}Fe^{3+}$ (B)	0.62 (1)	-0.01 (1)	44.9 (1)	0.65 (1)	66 (1)
150	Magnetite Fe^{3+} (A)	0.37 (1)	0.02 (1)	49.7 (1)	0.43 (1)	33 (1)
	Magnetite $Fe^{2+}Fe^{3+}$ (B)	0.69 (1)	0.00 (1)	46.7 (1)	0.70 (1)	67 (1)

resonant area ratio compatible, respectively, to the Fe^{3+} A sites and the $Fe^{2+/3+}$ B sites of the inverse spinel structure of the magnetite above the Verwey transition (T_V). Hyperfine parameters obtained from the fittings can be consulted in Table 2. The spectrum of the MNP-I collected at 295 K is considerably wider, and the hyperfine fields are significantly lower than those corresponding to the MNP-II. This variance is indicative that the MNP-I is close to a superparamagnetic state at room temperature.

In a stoichiometric bulk magnetite, the Verwey phase transition takes place at around 120 K and the inverse cubic (Fd3-m) spinel structure of magnetite reduces its symmetry and transforms into the monoclinic Cc structure. From 150 K, as the temperature decreases, the Mössbauer spectra of the studied samples show a slow evolution, in contrast with the expected sharp transition for a stoichiometric bulk magnetite. It has been observed that for magnetite MNPs, the Verwey phase transition can begin even at higher temperatures, extends in a broad temperature range, and is not completed down to lower temperatures [42]. At nanometric sizes, the relative increase of surface atoms with different chemical and structural topologies induces the formation of charge-ordered surface states which would include changes in the Verwey phase transition temperatures [43, 44], becoming more noticeable as the size of the MNPs lowers.

Below 150 K, the spectra cannot be properly described by a composition of only the spectral components of the stoichiometric Fe^{3+} A and $Fe^{2+/3+}$ B sites of the inverse spinel structure and more contributions would be needed for an appropriate fitting. The transition to the monoclinic structure gives rise to 24 different groups of Fe sites, 8 different groups of crystallographically equivalent A sites, and 16 different groups of crystallographically equivalent B sites. We have followed the fitting assignments described by Řezníček et al. [45] to fit the contribution of the monoclinic magnetite to the Mössbauer spectra of the studied samples. Based on

DFT calculations, they get a reliable simulation of the Mössbauer spectrum with a considerable agreement with of the experimental one. Concretely, they reduce the spectrum at temperatures below T_V to four sextets: two contributions representing Fe^{3+} from A position and Fe^{3+} from B-like position, respectively, and two spectra to describe the contribution of two different sets of Fe^{2+} from B-like position. So, the fitting of the Mössbauer spectra of samples below 150 K is composed of five different contributions, those describing the Fe^{3+} A and $Fe^{2+/3+}$ B sites of the inverse spinel structure above T_V and three describing the splitting of the $Fe^{2+/3+}$ B site in different crystallographic positions at lower temperatures. The aim of the analysis of the Mössbauer spectra in this work is not reinterpreting the structure of magnetite MNPs below T_V, and the results of the fittings will not be discussed. However, the description of the thermal evolution of the Mössbauer spectra is in line with a scenario of a broad cubic to monoclinic phase transition. As the temperature decreases, the relative contribution to the spectrum of the components assigned to the monoclinic phase increases at the expenses of the sextets corresponding to the spinel structure, becoming the main one at 77 K. It must be also underlined that the ratio among the resonant areas due to the Fe^{3+} A sites and the $Fe^{2+/3+}$ B sites remains around 1:2 which would corroborate the stoichiometry of the magnetite for all the temperatures.

4. Conclusions

A low-cost, easy, and reproducible method to obtain iron oxide superparamagnetic nanoparticles is presented. This method does not need sophisticated equipment and so is easy to reproduce anywhere. It is a low-cost, two-step method that allows the obtaining of two kinds of nanoparticles by thermal decomposition. In the first step, superparamagnetic nanoparticles of 9 ± 4 nm with a saturation

magnetization of 65 emu/g and a coercive field of 1 Oe are obtained; meanwhile, in the second step, the obtained nanoparticles with a size of 15 ± 5 nm present a saturation magnetization of 70 emu/g and a coercive field of 12 Oe.

Data Availability

The data used to support the findings of this study are included within the article.

Conflicts of Interest

The authors declare that they have no conflicts of interest.

Acknowledgments

References

[1] J. Govan and Y. Gun'ko, "Recent advances in the application of magnetic nanoparticles as a support for homogeneous catalysts," *Nanomaterials*, vol. 4, no. 2, pp. 222–241, 2014.

[2] G. Reiss and A. Hutten, "Applications beyond data storage," *Nature Materials*, vol. 4, no. 10, pp. 725-726, 2005.

[3] S. Chunming, "Environmental implications and applications of engineered nanoscale magnetite and its hybrid nanocomposites: A review of recent literature," *Journal of Hazardous Materials*, vol. 322, pp. 48–84, 2017.

[4] V. F. Cardoso, A. Francesko, C. Ribeiro, M. Bañobre-López, P. Martins, and S. Lanceros-Mendez, "Advances in magnetic nanoparticles for biomedical applications," *Advanced Healthcare Materials*, vol. 7, no. 5, p. 1700845, 2018.

[5] Y. Hu, S. Mignani, J. Majoral, M. Shen, and X. Shi, "Construction of iron oxide nanoparticle-based hybrid platforms for tumor imaging and therapy," *Chemical Society Reviews*, vol. 47, no. 5, pp. 1874–1900, 2018.

[6] J. Mosayebi, M. Kiyasatfar, and S. Laurent, "Synthesis, functionalization, and design of magnetic nanoparticles for theranostic applications," *Advanced Healthcare Materials*, vol. 6, no. 23, p. 1700306, 2017.

[7] H. Choi, W. Liu, P. Misra et al., "Renal clearance of quantum dots," *Nature Biotechnology*, vol. 25, no. 10, pp. 1165–1170, 2007.

[8] A. Tanimoto and S. Kuribayashi, "Application of superparamagnetic iron oxide to imaging of hepatocellular carcinoma," *European Journal of Radiology*, vol. 58, no. 2, pp. 200–216, 2006.

[9] S. M. Moghimi, "Mechanisms of splenic clearance of blood cells and particles: towards development of new splenotropic agents," *Advanced Drug Delivery Reviews*, vol. 17, no. 1, pp. 103–115, 1995.

[10] H. Cabral, Y. Matsumoto, K. Mizuno et al., "Accumulation of sub-100 nm polymeric micelles in poorly permeable tumours depends on size," *Nature Nanotechnology*, vol. 6, no. 12, pp. 815–823, 2011.

[11] S. D. Perrault, C. Walkey, T. Jennings, H. C. Fischer, and W. C. Chan, "Mediating tumor targeting efficiency of nanoparticles through design," *Nano Letters*, vol. 9, no. 5, pp. 1909–1915, 2009.

[12] R. B. Nasir Baig, M. N. Nadagouda, and R. S. Varma, "Magnetically retrievable catalysts for asymmetric synthesis," *Coordination Chemistry Reviews*, vol. 287, pp. 137–156, 2015.

[13] L. Li, Y. Yang, J. Ding, and J. Xue, "Synthesis of magnetite nanooctahedra and their magnetic field-induced two-/three-dimensional superstructure," *Chemistry of Materials*, vol. 22, no. 10, pp. 3183–3191, 2010.

[14] W. Wu, C. Z. Jiang, and V. A. L. Roy, "Designed synthesis and surface engineering strategies of magnetic iron oxide nanoparticles for biomedical applications," *Nanoscale*, vol. 8, no. 47, pp. 19421–19474, 2016.

[15] L. Douziech-Eyrolles, H. Marchais, K. Heme et al., "Nanovectors for anticancer agents based on superparamagnetic iron oxide nanoparticles," *International Journal of Nanomedicine*, vol. 2, no. 4, pp. 541–550, 2007.

[16] S. Laurent, D. Forge, M. Port et al., "Magnetic iron oxide nanoparticles: synthesis, stabilization, vectorization, physicochemical characterizations, and biological applications," *Chemical Reviews*, vol. 108, no. 6, pp. 2064–2110, 2008.

[17] D. Ling and T. Hyeon, "Chemical design of biocompatible iron oxide nanoparticles for medical applications," *Small*, vol. 9, no. 9-10, pp. 1450–1466, 2013.

[18] J. Park, K. An, Y. Hwang et al., "Ultra-large-scale syntheses of monodisperse nanocrystals," *Nature Materials*, vol. 3, no. 12, pp. 891–895, 2004.

[19] D. Kim, N. Lee, M. Park, B. H. Kim, K. An, and T. Hyeon, "Synthesis of uniform ferrimagnetic magnetite nanocubes," *Journal of the American Chemical Society*, vol. 131, no. 2, pp. 454-455, 2009.

[20] R. K. Sharma, S. Dutta, S. Sharma, R. Zboril, R. S. Varma, and M. B. Gawande, "Fe$_3$O$_4$ (iron oxide)-supported nanocatalysts: synthesis, characterization and applications in coupling reactions," *Green Chemistry*, vol. 18, no. 11, pp. 3184–3209, 2016.

[21] W. Jiang, K. Lai, K. Liu et al., ""Green" functionalization of magnetic nanoparticles via tea polyphenol for magnetic resonance/fluorescent dual-imaging," *Nanoscale*, vol. 6, no. 3, pp. 1305–1310, 2014.

[22] S. I. C. J. Palma, M. Marciello, A. Carvalho, S. Veintemillas-Verdaguer, M. P. Morales, and A. C. A. Roque, "Effects of phase transfer ligands on monodisperse iron oxide magnetic nanoparticles," *Journal of Colloid and Interface Science*, vol. 437, pp. 147–155, 2015.

[23] N. Lee, Y. Choi, Y. Lee et al., "Water-dispersible ferrimagnetic iron oxide nanocubes with extremely high r_2 relaxivity for highly sensitive in vivo MRI of tumors," *Nano Letters*, vol. 12, no. 6, pp. 3127–3131, 2012.

[24] V. M. Lenart, S. L. Gómez, M. P. Calatayud, and G. R. F. Goya, "Size and shape control of magnetite nanoparticles with a nonselective binding surfactants," 2014, http://arxiv.org/abs/1402.1134.

[25] A. R. Deniz, Z. Çaldıran, Ö. Metin, K. Meral, and S. Aydogan, "The investigation of the electrical properties of Fe$_3$O$_4$/_n_-Si heterojunctions in a wide temperature range," *Journal of Colloid and Interface Science*, vol. 473, pp. 172–181, 2016.

[26] Y. Lv, Y. Yang, J. Fang et al., "Size dependent magnetic hyperthermia of octahedral Fe3O4 nanoparticles," *RSC Advances*, vol. 5, no. 94, pp. 76764–76771, 2015.

[27] S. Sun, H. Zeng, D. B. Robinson et al., "Monodisperse MFe_2O_4 (M=Fe, Co, Mn) nanoparticles," *Journal of the American Chemical Society*, vol. 126, no. 1, pp. 273–279, 2004.

[28] P. Guardia, J. Pérez-Juste, A. Labarta, X. Batlle, and L. M. Liz-Marzán, "Heating rate influence on the synthesis of iron oxide nanoparticles: the case of decanoic acid," *Chemical Communications*, vol. 46, no. 33, pp. 6108–6110, 2010.

[29] T. H. de Keiiser and J. I. Langford, "Use of the Voigt function in a single-line method for the analysis of X-ray diffraction line broadening," *Journal of Applied Crystallography*, vol. 15, no. 3, pp. 308–314, 1982.

[30] S. G. Kwon and T. Hyeon, "Formation Mechanisms of Uniform Nanocrystals via Hot-Injection and Heat-Up Methods," *Small*, vol. 7, no. 19, pp. 2685–2702, 2011.

[31] S. J. Kemp, R. M. Ferguson, A. P. Khandhara, and K. M. Krishnanab, "Monodisperse magnetite nanoparticles with nearly ideal saturation magnetization," *RSC Advances*, vol. 6, no. 81, pp. 77452–77464, 2016.

[32] P. Guardia, N. Pérez, A. Labarta, and X. Batlle, "Controlled synthesis of iron oxide nanoparticles over a wide size range," *Langmuir*, vol. 26, no. 8, pp. 5843–5847, 2010.

[33] C. Fang, N. Bhattarai, C. Sun, and M. Zhang, "Functionalized nanoparticles with long-term stability in biological media," *Small*, vol. 5, no. 14, pp. 1637–1641, 2009.

[34] J. Santoyo, L. Pérez, O. De Abril et al., "Magnetic iron oxide nanoparticles in 10-40 nm range: composition in terms of magnetite/maghemite ratio and effect on the magnetic properties," *Chemistry of Materials*, vol. 23, no. 6, pp. 1379–1386, 2011.

[35] P. B. Shete, R. M. Patil, N. D. Thorat, A. Prasad, R. S. Ningthoujam, and S. J. Ghosh, "Magnetic chitosan nanocomposite for hyperthermia therapy application: preparation, characterization and in vitro experiments," *Applied Surface Science*, vol. 288, pp. 149–157, 2014.

[36] J. Rodríguez-Carvajal, "FullProf: a program from Rietveld refinement and pattern matching analysis," in *Abstract of the Satellite Meeting on Powder Diffraction of the XV Congress of the IUCr*, p. 127, Scientific Research, Toulouse, France, 1990.

[37] A. Le Bail, H. Duroy, and J. L. Fourquet, "Ab-initio structure determination of $LiSbWO_6$ by X-ray powder diffraction," *Materials Research Bulletin*, vol. 23, no. 3, pp. 447–452, 1988.

[38] S. G. Kwon, Y. Piao, J. Park et al., "Kinetics of monodisperse iron oxide nanocrystal formation by "heating-up" process," *Journal of the American Chemical Society*, vol. 129, no. 41, pp. 12571–12584, 2007.

[39] D. H. Han, J. P. Wang, Y. B. Feng, and H. L. Luo, "Influence of size and magnetocrystalline anisotropy on spin canting anomaly in fine ferrimagnetic particles," *Journal of Applied Physics*, vol. 76, no. 10, pp. 6591–6593, 1994.

[40] R. H. Kadama, "Magnetic nanoparticles," *Journal of Magnetism and Magnetic Materials*, vol. 200, no. 1-3, pp. 359–372, 1999.

[41] M. Bohra, N. Agarwal, and V. Singh, "A short review on Verwey transition in nanostructured Fe_3O_4 materials," *Journal of Nanomaterials*, vol. 2019, Article ID 8457383, 18 pages, 2019.

[42] I. Dézsi, C. S. Fetzer, Á. Gombkötő, I. Szűcs, J. Gubicza, and T. Ungár, "Phase transition in nanomagnetite," *Journal of Applied Physiology*, vol. 103, no. 10, article 104312, 2008.

[43] I. V. Shvetz, G. Mariotto, K. Jordan, N. Berdunov, R. Kantor, and S. Murphy, "Long-range charge order on theFe3O4(001)-surface," *Physical Review B*, vol. 70, no. 15, p. 155406, 2004.

[44] D. G. Mitchell, "MR imaging contrast agents — what's in a name?," *Journal of Magnetic Resonance Imaging*, vol. 7, no. 1, pp. 1–4, 1997.

[45] R. Řezníček, V. Chlan, H. Štěpánková et al., "Understanding the Mössbauer spectrum of magnetite below the Verwey transition:Ab initiocalculations, simulation, and experiment," *Physical Review B*, vol. 96, no. 19, p. 195124, 2017.